Impact of Atomic-Scale Contact Geometry on Andreev Reflection

J. Brand,[1,*] P. Ribeiro,[2] N. Néel,[1] S. Kirchner,[3] and J. Kröger[1]
[1]Institut für Physik, Technische Universität Ilmenau, D-98693 Ilmenau, Germany
[2]CeFEMA, Instituto Superior Técnico, Universidade de Lisboa, Av. Rovisco Pais, 1049-001 Lisboa, Portugal
[3]Center for Correlated Matter, Zhejiang University, Hangzhou, Zhejiang 310058, China
(Received 7 October 2016; published 9 March 2017)

Charge transport has been examined in junctions comprising the normal-metal tip of a low-temperature scanning tunneling microscope, the surface of a conventional superconductor, and adsorbed C_{60} molecules. The Bardeen-Cooper-Schrieffer energy gap gradually evolves into a zero-bias peak with decreasing electrode separation. The peak is assigned to the spectroscopic signature of Andreev reflection. The conductance due to Andreev reflection is determined by the atomic termination of the tip apex and the molecular adsorption orientation. Transport calculations unveil the finite temperature and the strong molecule-electrode hybridization as the origin to the surprisingly good agreement between spectroscopic data and the Blonder-Tinkham-Klapwijk model that was conceived for macroscopic point contacts.

DOI: 10.1103/PhysRevLett.118.107001

Andreev reflection (AR) occurs at the interface of a superconductor (S) and a normal metal (N) [1]. An electron incident from N with Fermi wavelength much smaller than the coherence length of S is retroreflected at the S–N interface as a phase-conjugated hole while simultaneously creating a Cooper pair in S. The observation of AR in S–N and multiple AR in S–S contacts has considerably influenced our understanding of electron transport through these kind of junctions. In addition, AR is considered the microscopic origin to the superconducting proximity effect [2]. Multiple AR was demonstrated to represent an appropriate means of identifying transmission probabilities of electron transport channels in atomic S–S junctions [3]. Furthermore, AR is at the base of tunable supercurrents through semiconductor nanowires contacted by S electrodes [4], electron transport through graphene quantum dots [5], and correlated spin currents in topological superconductors [6].

The majority of AR experiments was performed with macroscopic point contacts [7], while systematic studies of AR based on a scanning tunneling microscope (STM) are scarce. The first STM experiment unveiling AR was performed on polycrystalline Pb as well as on crystalline Au surfaces using Au, Pb, and Pt-Rh tips [8]. At junction resistances of several Ohms, a zero-bias peak was observed in spectra of the differential conductance (dI/dV) and interpreted as the signature of AR [8]. The low-Ohmic contacts resulted from strong tip indentations into the substrate material, leaving behind deteriorated tip and surface structure. In a more recent STM experiment, a W tip and the superconductor V_3Si [9] were used. With an increasing current across the junction, the Bardeen-Cooper-Schrieffer (BCS) energy gap was reduced, which was substantiated in terms of AR [9]. Multiple AR was studied as a function of electrode separation [10] and utilized to infer the number of transport channels and their transmission coefficients of C_{60} adsorbed on Pb(111) [11]. However, AR in single-atom and single-molecule S–N junctions with atomic-scale imaging prior to and after contact formation has not been reported to date. The pertinent question of how the atomic electrode geometry and interface structure of such junctions affects AR has thus far remained open. Moreover, spectroscopy experiments with an STM enable the unambiguous identification of AR by tuning the junction from the tunneling to the contact range [12,13] and therefore, its discrimination from other zero-bias features [14].

We used a low-temperature STM to fabricate single-atom and single-molecule junctions [15,16] with a W tip and a single-crystalline surface of Nb. Spectra of dI/dV were acquired for junctions comprised of pristine W tips, single Nb atoms ($W-Nb$), and single C_{60} molecules ($W-C_{60}$), as well as C_{60}-terminated W tips and single Nb atoms ($C_{60}-Nb$). In the tunneling range, all junctions exhibited the BCS energy gap with a zero-Kelvin gap width Δ_0 and a critical temperature T_c that were virtually identical to the values of bulk Nb. Upon decreasing the electrode separation, the BCS energy gap gradually evolved into a zero-bias peak, which is assigned to AR. Experimental observations and theoretical modeling evidence the dependence of the AR-induced conductance on atomic-scale details of the electrode geometry. Unexpectedly, the Blonder-Tinkham-Klapwijk (BTK) model [12] that was originally conceived for macroscopic point contacts describes the experimental data observed from single-atom and single-molecule junctions very well. The main origin to this surprising behavior is the finite temperature and the coupling of the atoms and molecules to the electrodes.

Experiments were performed with a STM operated at 5.5 K and at 10^{-9} Pa. The Nb(110) surface was prepared by

annealing between 2200 and 2650 K [17]. High-purity (99.95%) W wire was used as the tip material. C_{60} molecules were sublimated in an ultrahigh vacuum and deposited onto the sample at room temperature. The termination of tip apices with single C_{60} molecules was achieved using standard procedures [22]. STM images were acquired at constant current with the bias voltage applied to the sample. Spectra of dI/dV were recorded by a lock-in technique.

The surface of the Nb(110) crystal imaged with a W tip [Fig. 1(a)] exhibits a characteristic pattern of parallel atomic chains [Fig. 1(b)]. The individual atoms that are visible as circular protrusions in the STM image are Nb atoms, which terminate the NbO(111) monolayer on Nb(110) [18].

Adsorbed C_{60} molecules [Fig. 1(c)] appear with a variety of submolecular patterns [Fig. 1(d)]. Depending on the bias voltage, these patterns are due to the highest occupied molecular orbital (HOMO) and the lowest unoccupied molecular orbital (LUMO) [24,25]. The variety of structural motifs observed in STM images acquired with a W tip therefore reflects different C_{60} adsorption configurations.

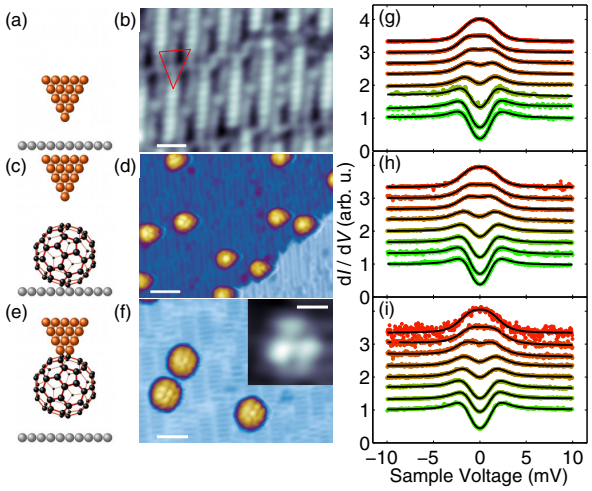

FIG. 1. (a) Sketch of a W – Nb junction. (b) STM image of Nb atom chains on NbO(111) (100 mV, 500 nA, scale bar: 1 nm). The triangle indicates the preferred C_{60} adsorption region. (c) Sketch of a W – C_{60} junction. (d) STM image of individual C_{60} molecules adsorbed on NbO(111) (100 mV, 50 pA, scale bar: 3 nm). C_{60} molecules appear as circular protrusions with submolecular structure. (e) Sketch of a C_{60} – Nb junction. (f) STM image of individual C_{60} molecules on NbO(111) acquired with a C_{60}-terminated tip (100 mV, 50 pA, scale bar: 2 nm). Inset: STM image of an atomic protrusion on the surface revealing the C_{60} orientation at the tip apex (100 mV, 50 pA, scale bar: 0.5 nm). (g)–(i) Normalized dI/dV spectra (dots) of W – Nb (g), W – C_{60} (h), C_{60} – Nb (i) junctions with decreasing electrode separation (from bottom to top). Junction conductances range from (g) 0.20 to 1.29 G_0, (h) 0.11 to 1.35 G_0, (i) 0.34 to 0.97 G_0. Spectra are offset vertically for clarity. Full lines represent fits according to the BTK model. The color of the data sets reflects the magnitude of the BTK transmission τ (green: $\tau = 0$, red: $\tau = 1$).

The controlled termination of the W tip apex with a single C_{60} molecule [Fig. 1(e)] was routinely performed [22]. STM images of the C_{60}-covered surface acquired with the C_{60}-terminated tip [Fig. 1(f)] gave rise to even more complex structural motifs of adsorbed C_{60}, which are in agreement with a recent study [25]. Following earlier reports [26,27], the tip apex was imaged by an atomic defect on the surface [inset to Fig. 1(f)], which enables the determination of the C_{60} orientation at the tip [28]. In the case of the inset to Fig. 1(f), the C_{60} at the tip apex gave rise to a cloverlike pattern in STM images, which is indicative of a C hexagon exposed to the surface.

For all junctions dI/dV spectroscopy was performed as a function of the tip–sample separation [Figs. 1(g)–1(i)]. The resulting junction conductances cover tunneling and contact ranges [29]. In the tunneling range, all junctions exhibit a depletion of dI/dV around 0 mV, flanked by symmetrically positioned peaks at $\approx \pm 3$ mV. This feature is assigned to the broadened BCS energy gap. Tunneling spectroscopic data were fit by the BCS expression for the quasiparticle density of states (DOS), $\varrho(E) = \varrho_0 |E|/\sqrt{E^2 - \Delta^2}$ (E: energy of the quasiparticle state, Δ: half width of the BCS energy gap), considering the finite temperature as well as the broadening due to the voltage modulation [38]. The fits are shown as the full lines in the bottom spectra of Figs. 1(g)–1(i).

Increasing the sample temperature led to a gradual reduction of the width and depth of the dI/dV depletion [38]. The experimentally inferred temperature dependence of Δ is in agreement with predictions by BCS theory. From the fit of experimental data, Δ_0 and T_c were extracted. Tunneling into single Nb atoms (C_{60} molecules) resulted in $\Delta_0 = 1.52 \pm 0.01$ meV, $T_c = 9.21 \pm 0.05$ K ($\Delta_0 = 1.54 \pm 0.02$ meV, $T_c = 9.20 \pm 0.12$ K). Within the uncertainty margins, the C_{60} junctions do not differ from W – Nb junctions with respect to Δ_0 and T_c. Moreover, Δ_0 and T_c obtained for all junctions are in agreement with Δ_0 and T_c that were previously observed in tunneling experiments with pristine Nb samples [39].

In a next step, dI/dV spectra of the junctions were acquired at decreasing electrode distances. All junctions exhibited similar behavior. The BCS energy gap gradually evolved into a zero-bias peak for junction conductances well in the contact range. Importantly, the contact regions were imaged prior to and after contact in order to identify atomic-scale modifications of the electrode geometry. Only those dI/dV data entered the subsequent analysis that corresponded to junctions with no changes due to contact. Experiments at 10 K, i.e., at a temperature larger than T_c of Nb, revealed the absence of the BCS gap and of the zero-bias peak. These experimental results further support the interpretation of the zero-bias peak as the spectroscopic signature of AR.

Unexpectedly, dI/dV data acquired for junctions with various geometries and tip-sample separations ranging

from tunneling to contact ranges are well described by the BTK model [full lines in Figs. 1(g)–1(i)]. In the BTK model, the tunneling barrier separating the two electrodes is modeled as a Dirac δ function of weight Z. The S–N junction is characterized by its normal-state transmission, $\tau = 1/(1+Z^2)$, and the effective area, $\mathcal{A}$. $Z \to \infty$ ($Z = 0$) mimics the tunneling (contact) range. In the limit of infinite barrier strength, BTK theory reproduces the BCS energy gap. For multiple AR observed from C_{60} contacts on Pb(111) with a Nb tip, the Landauer-Büttiker approach [45,46] was used to describe the subharmonic gap structure in current-voltage characteristics [11].

The spectroscopic data [Figs. 1(g)–1(i)] evidence the impact of the specific junction geometry on AR. To see this effect, τ was plotted as a function of the normal-state differential conductance, dI/dV_n [Figs. 2(a)–2(c)], which reflects the junction dI/dV evaluated at sample voltages $V \gg \Delta_0/e$. All junctions exhibited a linear variation of τ with dI/dV_n in line with the BTK model. Figures 2(a)–2(c) evidence that the data grouped around linear variations with distinct slopes. In the BTK model, different slopes of τ may hint at different effective contact areas $\mathcal{A}$. For single-atom and single-molecule junctions, the different slopes may result from different numbers of transport channels and/or transmission probabilities of each channel [45,46].

For W – Nb junctions, the data presented in Fig. 2(a) were best described by linear fits, $\tau = \chi_{1,2} dI/dV_n$, with $\chi_1 = 0.86 \pm 0.02\ G_0^{-1}$ (upper line, $G_0 = 2e^2/h$ is the quantum of conductance with e the elementary charge and h the Planck constant) and $\chi_2 = 0.44 \pm 0.03\ G_0^{-1}$ (bottom line); i.e., for a given τ, the differential conductance, dI/dV_n, differed by a factor of nearly 2. Consequently, the different slopes in Fig. 2(a) are assigned to the termination of the tip with a single (χ_1) and with two (χ_2) W atoms. This assignment is corroborated by STM images of the contact area. While tips leading to τ traces with the larger slope gave rise to atomically resolved STM images of Nb chains, STM images acquired with the other kind of tips appeared rather blurred. This blurred appearance of STM images is indicative of tips that are not terminated by a single atom. In addition, the concomitant doubling of the junction conductance was reported by changing contacts from monatomic to diatomic clusters on metal surfaces [27].

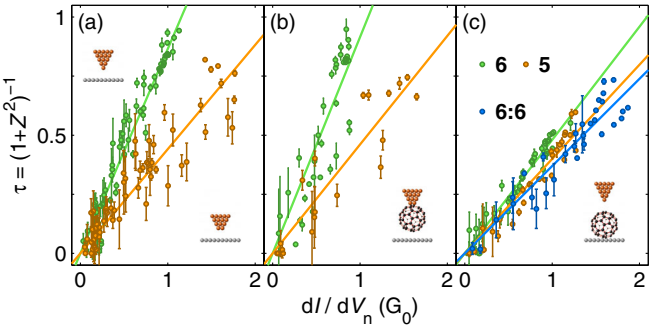

FIG. 2. Variation of τ as a function of dI/dV_n evaluated at ± 10 mV for (a) W – Nb, (b) C_{60} – Nb, (c) W – C_{60} junctions. Depending on the junction geometry, experimental data grouped around linear τ variations with different slopes. In (a) the variation with the higher (lower) slope reflects data acquisition with a W tip terminated by a single atom (two atoms). In (b) the higher (lower) slope was obtained for the tip approaching a single Nb atom (the region between two Nb atom rows). In (c) different slopes were obtained for **6**, **5**, **6**:**6** C_{60} orientations.

In similar experiments, C_{60} – Nb junctions were explored [Fig. 2(b)]. Contacts to a single Nb atom embedded in a monatomic chain and contacts to the trench between two adjacent Nb chains led to linear variations of τ with a slope of $0.91 \pm 0.19\ G_0^{-1}$ and $0.46 \pm 0.10\ G_0^{-1}$, respectively. Consequently, C_{60} – Nb junctions comprising Nb atoms of adjacent chains exhibited conductances being a factor ≈ 2 larger than conductances obtained from single-Nb junctions.

W – C_{60} junctions showed linear τ evolutions with less distinct slopes [Fig. 2(c)]. The different slopes were related to different orientations of adsorbed C_{60} molecules. While a variety of structural motifs were observed from adsorbed C_{60} molecules, we concentrate here on the most frequently observed patterns, that is, **6**, **5**, **6**:**6** exposing a C hexagon, a C pentagon, a C–C bond between two adjacent C hexagons to the vacuum, respectively [24]. The lowest differential conductance at any given τ was observed for **6** with a slope of $\chi_{\mathbf{6}} = 0.48 \pm 0.04\ G_0^{-1}$, followed by **5** with $\chi_{\mathbf{5}} = 0.40 \pm 0.02\ G_0^{-1}$ and **6**:**6**, with $\chi_{\mathbf{6:6}} = 0.37 \pm 0.02\ G_0^{-1}$. Previously, conductances beyond the point of contact varied in the same way with the C_{60} orientation [30] as reported here for the transmission in the presence of AR.

Before entering into the modeling of the experimental data, a few general statements on electron transport through S–N contacts are noteworthy. For a single-channel S–N contact, the junction conductance may be decomposed into contributions from AR and conventional electron transport. In the generic case of several contributing transport channels, the disentanglement of AR requires the knowledge of all transmission coefficients. However, the present situation is fortunate. The size of the HOMO–LUMO gap and the smooth bias voltage dependence of dI/dV data [47] imply that the DOS is essentially independent of the energy at the Fermi level, E_F. Therefore, a general expression relates the S–N junction conductance to the transmission of transport channels [13]. Further simplifications arise for a point contact with a high number of transport channels. In this case, the BTK model proved the systematic disentanglement of AR from the total conductance of a S–N junction [12,54].

In the present case where only a small number of transport channels participate, neither the single-channel result nor the BTK expression for the conductance are

per se applicable. Moreover, the general results of Ref. [13] and their extension to finite bias voltage would require knowledge of all channel transmissions. This would seem to require an *ab initio* modeling of the junction. However, Figs. 1(g)–1(f) evidence the accordance between dI/dV data and the BTK model.

In the following, we first rationalize the surprisingly good quality of BTK fits to experimental data and then explore the impact of the atomic-scale electrode geometry on AR by comparison with transport calculations. The simulations are similar to previously reported methods [13]. The Hamiltonian, $H = H_S + H_N + H_M + H_{MS} + H_{MN}$, considers the contribution of the superconducting (H_S) and normal-metal (H_N) electrodes, the molecule (H_M), as well as its coupling to the superconductor (H_{MS}) and the normal metal (H_{MN}) to the total energy. The molecule (M) is characterized by a single-particle energy level ε_d with respect to E_F of the leads at zero voltage. The coupling of M to the electrodes is described by the hybridization energies $\Gamma_S = \pi t^2 \varrho_0$ and $\Gamma_N = \pi \tilde{t}^2 \tilde{\varrho}_0$ [ϱ_0 ($\tilde{\varrho}_0$): DOS of S (N) in the nonsuperconducting phase at E_F, t ($\tilde{t}$): hopping amplitude from M to S (N)]. Electron transport through the junction was then obtained by solving the equation of motion for the nonequilibrium Green function on the Keldysh contour in Nambu space [38].

As a first result, we obtained that for $\Gamma_S \gg \Delta, \varepsilon_d, eV$ or $\Gamma_N \gg \Delta, \varepsilon_d, eV$, the internal electronic structure of M was considerably broadened and the BTK expression for the current was recovered with $Z = |\Gamma_S - \Gamma_N|/\sqrt{2\Gamma_S\Gamma_N}$ [38].

In a next step, we addressed the validity of the BTK model for a junction with a few transport channels. To capture the basic physics, a model was conceived where M is adsorbed to S with a hybridization $\Gamma_S \gg \Delta, \varepsilon_d, eV$ [Fig. 3(a)]. Two parallel transport channels, α and β, were included in the calculations. Their different transmissions were mimicked by different couplings to N, $\Gamma_N^{(\alpha)}$ and $\Gamma_N^{(\beta)}$. Figures 3(b),(c) present calculated dI/dV data for a molecular junction with $\gamma_N = \Gamma_N^{(\beta)}/\Gamma_N^{(\alpha)} = 0.2$ at $T = 0$ K [Fig. 3(b)] and at $T = 0.3\Delta_0/k_B \approx 5.3$ K (k_B: Boltzmann constant) with $\Delta_0 = 1.53$ meV being the average of experimentally determined gap widths [Fig. 3(c)]. The dots represent data obtained from the microscopic model, while the full lines are fits according to the BTK model. At 0 K, discrepancies between the microscopic model and the BTK approach became discernible at elevated τ. However, our calculations revealed that good agreement between the transport calculations and the BTK model is achieved for temperatures starting from as low as $0.05T_c$. Both models were in excellent agreement for all τ at finite temperatures $> 0.05T_c$. Similar results were obtained for $\gamma_N = 0.1, 0.5$ (not shown). These data suggest that the finite temperature of the junction likewise contributes to the good BTK fit results exposed in Figs. 1(g)–1(i).

Figure 3(d) shows another important result, which concerns the applicability of the BTK model to situations

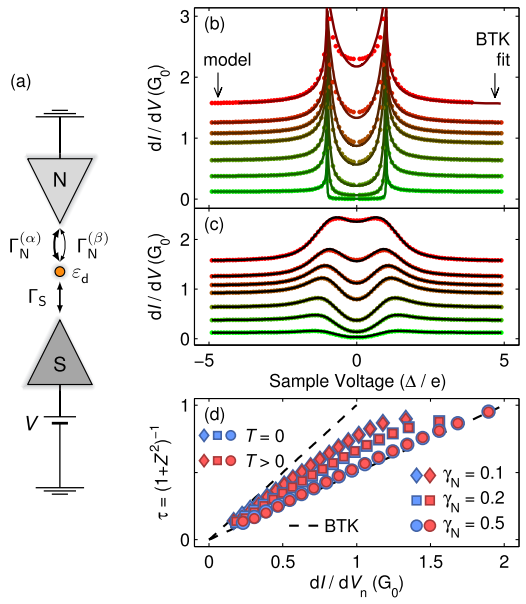

FIG. 3. (a) Sketch of the model used for transport calculations. The molecule is represented by a single electronic level ε_d. $\Gamma_N^{(\alpha)}$, $\Gamma_N^{(\beta)}$ denote coupling strengths of the two transport channels with the N electrode. Γ_S is the hybridization of the single transport channel to the S electrode. (b) Calculated dI/dV data (dots) for $\gamma_N = \Gamma_N^{(\beta)}/\Gamma_N^{(\alpha)} = 0.2$ and $T = 0$ K. Full lines are fits to calculated data on the basis of the BTK model. The color of the lines encodes the normal-state transmission of $\tau^{(\alpha)} > \tau^{(\beta)}$ (green: $\tau^{(\alpha)} = 0$, red: $\tau^{(\alpha)} = 1$). (c) Like (b) for $T = 0.3\Delta_0/k_B$ with $\Delta_0 = 1.53$ meV the average of experimentally determined gap widths. (d) τ extracted from single-channel BTK fits to calculated dI/dV data as a function of dI/dV_n. The upper (lower) dashed line represents $\tau = 1.0 \cdot G_0^{-1}\, dI/dV_n$ ($\tau = 0.5 \cdot G_0^{-1}\, dI/dV_n$).

where several transport channels with different transmissions are involved. Within the microscopic model dI/dV data were calculated for $\gamma_N = 0.1$, 0.2, 0.5 and different temperatures ($T = 0$ K, $T = 0.3\Delta_0/k_B$). These calculated data were fit on the basis of the single-channel BTK model. The extracted transmission [symbols in Fig. 3(d)] shows distinct variations, which depend on γ_N. These variations are similar to the experimental observations depicted in Figs. 2(a)–2(c). Therefore, given the maximum conductance of 1 G_0 per transport channel, the minimum number of channels m may be inferred from the intersection of $\tau = 1$ with linearly extrapolated τ-versus-dI/dV_n data, which gives rise to $dI/dV_n \geq m\, G_0$.

In conclusion, AR in microscopic S–N junctions depends on the atomic-scale electrode geometry. The BTK model is excellently applicable to single-atom and single-molecule junctions when a finite temperature and a strong molecule–electrode coupling are present. The phenomenological BTK parameter Z is related to the hybridization constants. Moreover, the findings represent a new way of determining the minimum number of transport channels involved in the charge transport across the S–N

contact. The results further constitute a necessary first step in addressing the interplay of AR with spin-flip scattering at the nanoscale [55] and are anticipated to describe AR in single-atom and single-molecule junctions on high-T_c superconductors.

Funding by the Deutsche Forschungsgemeinschaft through Grant No. KR 2912/10-1 is acknowledged. J. B., N. N. and J. K. thank Dr. Christoph Sürgers, Professor José I. Pascual and Professor Erich Runge for discussions. P. R. thanks for support by FCT through the Investigador FCT contract IF/00347/2014. S. K. acknowledges partial support by the National Science Foundation of China, Grant No. 11474250 and the National Key R&D Program of the MOST of China (No. 2016YFA0300202).

*jonathan.brand@tu-ilmenau.de

[1] A. F. Andreev, Sov. Phys. JETP **19**, 1228 (1964).
[2] B. Pannetier and H. Courtois, J. Low Temp. Phys. **118**, 599 (2000).
[3] E. Scheer, N. Agraït, J. C. Cuevas, A. L. Yeyati, B. Ludoph, A. Martín-Rodero, G. R. Bollinger, J. M. van Ruitenbeek, and C. Urbina, Nature (London) **394**, 154 (1998).
[4] Y.-J. Doh, J. A. van Dam, A. L. Roest, E. P. A. M. Bakkers, L. P. Kouwenhoven, and S. D. Franceschi, Science **309**, 272 (2005).
[5] T. Dirks, T. L. Hughes, S. Lal, B. Uchoa, Y.-F. Chen, C. Chialvo, P. M. Goldbart, and N. Mason, Nat. Phys. **7**, 386 (2011).
[6] J. J. He, J. Wu, T.-P. Choy, X.-J. Liu, Y. Tanaka, and K. T. Law, Nat. Commun. **5**, 3232 (2014).
[7] N. Agraït, A. L. Yeyati, and J. M. van Ruitenbeek, Phys. Rep. **377**, 81 (2003).
[8] N. Agraït, J. G. Rodrigo, and S. Vieira, Phys. Rev. B **46**, 5814 (1992).
[9] N. Hauptmann, M. Becker, J. Kröger, and R. Berndt, Phys. Rev. B **79**, 144522 (2009).
[10] M. Ternes, W.-D. Schneider, J.-C. Cuevas, C. P. Lutz, C. F. Hirjibehedin, and A. J. Heinrich, Phys. Rev. B **74**, 132501 (2006).
[11] R. Hiraoka, R. Arafune, N. Tsukahara, M. Kawai, and N. Takagi, Phys. Rev. B **90**, 241405 (2014).
[12] G. E. Blonder, M. Tinkham, and T. M. Klapwijk, Phys. Rev. B **25**, 4515 (1982).
[13] C. W. J. Beenakker, Phys. Rev. B **46**, 12841 (1992).
[14] H.-H. Sun, K.-W. Zhang, L.-H. Hu, C. Li, G.-Y. Wang, H.-Y. Ma, Z.-A. Xu, C.-L. Gao, D.-D. Guan, Y.-Y. Li, C. Liu, D. Qian, Y. Zhou, L. Fu, S.-C. Li, F.-C. Zhang, and J.-F. Jia, Phys. Rev. Lett. **116**, 257003 (2016).
[15] J. Kröger, N. Néel, and L. Limot, J. Phys. Condens. Matter **20**, 223001 (2008).
[16] R. Berndt, J. Kröger, N. Neel, and G. Schull, Phys. Chem. Chem. Phys. **12**, 1022 (2010).
[17] See Supplemental Material at http://link.aps.org/supplemental/10.1103/PhysRevLett.118.107001, which includes Refs. [18–21], for details of sample preparation and surface characteristics.
[18] C. Wolf and U. Köhler, Thin Solid Films **500**, 347 (2006).
[19] C. Sürgers, M. Schöck, and H. v. Löhneysen, Surf. Sci. **471**, 209 (2001).
[20] A. S. Razinkin, E. V. Shalaeva, and M. V. Kuznetsov, Phys. Met. Metallogr. **106**, 56 (2008).
[21] A. Razinkin and M. Kuznetsov, Phys. Met. Metallogr. **110**, 531 (2010).
[22] See Supplemental Material at http://link.aps.org/supplemental/10.1103/PhysRevLett.118.107001, which includes Ref. [23], for termination of the tip with a single C_{60} molecule.
[23] G. Schull, T. Frederiksen, M. Brandbyge, and R. Berndt, Phys. Rev. Lett. **103**, 206803 (2009).
[24] I. D. Hands, J. L. Dunn, and C. A. Bates, Phys. Rev. B **81**, 205440 (2010).
[25] A. J. Lakin, C. Chiutu, A. M. Sweetman, P. Moriarty, and J. L. Dunn, Phys. Rev. B **88**, 035447 (2013).
[26] K. F. Kelly, D. Sarkar, S. Prato, J. S. Resh, G. D. Hale, and N. J. Halas, J. Vac. Sci. Technol. B **14**, 593 (1996).
[27] G. Schull, T. Frederiksen, A. Arnau, D. Sánchez-Portal, and R. Berndt, Nat. Nanotechnol. **6**, 23 (2011).
[28] See Supplemental Material at http://link.aps.org/supplemental/10.1103/PhysRevLett.118.107001, which includes Refs. [24,25], for inferring the C_{60} orientation from molecular structural motifs in STM images.
[29] See Supplemental Material at http://link.aps.org/supplemental/10.1103/PhysRevLett.118.107001, which includes Refs. [30–37], for details of the fabrication and characterization of single-atom and single-molecule contacts with an STM.
[30] N. Néel, J. Kröger, L. Limot, and R. Berndt, Nano Lett. **8**, 1291 (2008).
[31] L. Limot, J. Kröger, R. Berndt, A. Garcia-Lekue, and W. A. Hofer, Phys. Rev. Lett. **94**, 126102 (2005).
[32] N. Néel, J. Kröger, L. Limot, K. Palotas, W. A. Hofer, and R. Berndt, Phys. Rev. Lett. **98**, 016801 (2007).
[33] N. Néel, J. Kröger, and R. Berndt, Phys. Rev. Lett. **102**, 086805 (2009).
[34] J. Kröger, H. Jensen, and R. Berndt, New J. Phys. **9**, 153 (2007).
[35] N. Néel, J. Kröger, L. Limot, T. Frederiksen, M. Brandbyge, and R. Berndt, Phys. Rev. Lett. **98**, 065502 (2007).
[36] N. Néel, L. Limot, J. Kröger, and R. Berndt, Phys. Rev. B **77**, 125431 (2008).
[37] N. Hauptmann, F. Mohn, L. Gross, G. Meyer, T. Frederiksen, and R. Berndt, New J. Phys. **14**, 073032 (2012).
[38] See Supplemental Material at http://link.aps.org/supplemental/10.1103/PhysRevLett.118.107001, which includes Refs. [12,39–44], for the description of experimental spectroscopic data using the BCS and BTK model together with instrumental and thermal broadening.
[39] P. Townsend and J. Sutton, Phys. Rev. **128**, 591 (1962).
[40] I. Giaever and K. Megerle, Phys. Rev. **122**, 1101 (1961).
[41] J. Bardeen, L. N. Cooper, and J. R. Schrieffer, Phys. Rev. **108**, 1175 (1957).
[42] J. Bardeen, Phys. Rev. Lett. **6**, 57 (1961).
[43] V. Lukic, Ph. D. thesis, University of Illinois at Urbana-Champaign, 2005.
[44] Y. de Wilde, T. Klapwijk, A. Jansen, J. Heil, and P. Wyder, Physica B (Amsterdam) **218B**, 165 (1996).

[45] R. Landauer, IBM J. Res. Dev. **1**, 223 (1957).
[46] M. Büttiker, IBM J. Res. Dev. **32**, 63 (1988).
[47] See Supplemental Material at http://link.aps.org/supplemental/10.1103/PhysRevLett.118.107001, which includes Refs. [48–53], for a description of the C_{60} orbital electronic structure.
[48] J. A. Stroscio, R. M. Feenstra, and A. P. Fein, Phys. Rev. Lett. **57**, 2579 (1986).
[49] G. Géranton, C. Seiler, A. Bagrets, L. Venkataraman, and F. Evers, J. Chem. Phys. **139**, 234701 (2013).
[50] K. J. Franke, G. Schulze, N. Henningsen, I. Fernández-Torrente, J. I. Pascual, S. Zarwell, K. Rück-Braun, M. Cobian, and N. Lorente, Phys. Rev. Lett. **100**, 036807 (2008).
[51] X. Yao, T. G. Ruskell, R. K. Workman, D. Sarid, and D. Chen, Surf. Sci. **366**, L743 (1996).
[52] G.-C. Liang and A. W. Ghosh, Phys. Rev. Lett. **95**, 076403 (2005).
[53] R. Hesper, L. H. Tjeng, and G. A. Sawatzky, Europhys. Lett. **40**, 177 (1997).
[54] G. E. Blonder and M. Tinkham, Phys. Rev. B **27**, 112 (1983).
[55] E. J. H. Lee, X. Jiang, R. Aguado, G. Katsaros, C. M. Lieber, and S. De Franceschi, Phys. Rev. Lett. **109**, 186802 (2012).